Journal of Catalysis **204,** 129–145 (2001)
doi:10.1006/jcat.2001.3383, available online at http://www.idealibrary.com on IDEAL®

Relationship between the Structure/Composition of Co–Mo Catalysts and Their Ability to Produce Single-Walled Carbon Nanotubes by CO Disproportionation

Jose E. Herrera, Leandro Balzano, Armando Borgna,[1] Walter E. Alvarez, and Daniel E. Resasco[2]

School of Chemical Engineering and Materials Science, University of Oklahoma, 100 E. Boyd St., Norman, Oklahoma 73019

Received March 28, 2001; revised August 10, 2001; accepted August 10, 2001

A series of analytical techniques have been employed to fully characterize the structure and chemical state of Co–Mo/SiO_2 catalysts used for the production of single-walled carbon nanotubes (SWNT) by CO disproportionation at 700–850°C. The state of Co and Mo on a series of silica-supported catalysts was investigated using extended X-ray absorption fine structure, X-ray absorption near-edge spectroscopy, ultraviolet–visible diffuse reflectance spectroscopy, H_2 temperature-programmed reduction, X-ray photoelectron spectroscopy, and diffuse reflectance Fourier transform infrared spectroscopy of adsorbed NO after two sequential pretreatments and after the production of SWNT under pure CO. It was found that the selectivity of the Co–Mo catalysts toward SWNT strongly depends on the stabilization of Co species in a nonmetallic state before exposure to CO, which results from an interaction with Mo. The extent of this interaction is a function of the Co : Mo ratio and has different forms during the different stages of the catalyst life. From the detailed characterization conducted over the catalyst series it is concluded that after calcination, Mo is in the form of a well-dispersed Mo(6+) oxide while Co is either interacting with Mo in a superficial Co molybdatelike structure (at low Co : Mo ratios) or as a noninteracting Co_3O_4 phase (at high Co : Mo ratios). After a subsequent treatment in hydrogen, the noninteracting phase is reduced to metallic Co, while the Co molybdate-like species remain as well-dispersed Co^{2+} ions. During the production of SWNT under pure CO, the Mo oxide species are converted into Mo carbide. This conversion disrupts the interaction between Co and Mo and results in the release of metallic Co in the form of extremely small clusters, which are responsible for the production of SWNT. By contrast, large Co clusters that are formed from the noninteracting Co phase produce the nonselective forms of carbon (multiwalled nanotubes, filaments, graphite, etc.).

1. INTRODUCTION

The single-wall carbon nanotubes (SWNT) exhibit exceptional chemical and physical properties that have opened a vast number of potential applications (1). Among the various alternatives investigated in the last few years for production of SWNT, the catalytic decomposition of carbon-containing molecules appears to be a promising technique since it has the potential to be scaled-up at relatively low cost. A number of researchers have investigated different catalyst formulations and operating conditions for this process (2, 3). Our group has focused on the disproportionation of CO on several bimetallic catalysts, which exhibited a high selectivity toward the production of SWNT at relatively low temperatures. Among the various formulations investigated, Co–Mo catalysts supported on silica gel and having low Co : Mo ratios exhibited the best performance (4).

The Co-Mo system is well-known in the field of catalysis due to its application in hydrotreating catalytic processes. In that case, however, silica is not the most suitable support, due to its weak interaction with the active components. Most studies on the Co–Mo catalysts have focused on alumina-supported systems, since alumina interacts with Co and Mo with the appropriate strength to generate HDS active species. For that reason, alumina-supported Co-Mo catalysts are used in industry in the form of sulfides. Although the structure of the sulfided Co-Mo catalysts is known almost at the atomic level (5–8), that of the nonsulfided oxidic precursor has received less attention (9–12). Topsøe and Topsøe (13), using infrared (IR) spectroscopy of adsorbed NO showed that the interaction between Mo and the alumina in the oxidic state was not greatly affected by the presence of Co. A similar conclusion was reached by Ratnasami and Knözinger (9), who used IR and ultraviolet–visible (uv–vis) diffuse reflectance spectroscopy (DRS) to infer that in the oxidic state, a major portion of the Co is inside the alumina lattice in a tetrahedral environment of oxygen ions and is not exposed to the gas phase. Silica-supported Co-Mo, which is the system of our interest, displays a different behavior from that of the alumina-supported catalysts (13–18). The differences have been attributed to the lower affinity of silica for the Co and Mo ions, thus facilitating the Co-Mo interaction. The exact nature of this interaction is still unclear. While some authors

[1] Permanent address: INCAPE, Universidad Nacional del Litoral, Santiago del Estero 2654, Santa Fe, Argentina.

[2] To whom correspondence should be addressed. E-mail: resasco@ou.edu.

0021-9517/01 $35.00

have postulated that the interacting phase is different from cobalt molybdate (13, 15, 16), others have argued that a $CoMoO_4$ phase is indeed present (14, 17, 18).

As mentioned above, we have found that the silica-supported Co-Mo system displays very high selectivity in the production of SWNT by CO disproportionation (19). It is interesting to note that the high yields and selectivities to SWNT were only obtained after a specific sequence of calcination at 500°C in air and reduction in H_2 at 500°C, followed by heating in He to 700°C. Therefore, we have focused our attention on the characterization of the different phases and surface species present in this system after each of these two pretreatments and after the production of SWNT. In this contribution, we have used a variety of characterization techniques, including extended X-ray absorption fine structure (EXAFS), X-ray absorption near-edge spectroscopy (XANES), UV–vis DRS, H_2-TPR (temperature-programmed reduction) X-ray photoelectron spectroscopy (XPS), and diffuse reflectance Fourier transform infrared (DRIFTS) of NO adsorbed, which provide complementary information.

We have designed our characterization strategy on the basis of the abundant precedent literature on the application of these techniques to investigate the Co-Mo system. For example, UV–vis spectroscopy has been previously used to estimate the domain size of transition metal oxides (mostly d^0 ions) by analyzing the absorption edge energy according to the method proposed by Weber (20). Similarly, the IR spectroscopy of adsorbed NO has been widely used to characterize the Co-Mo catalytic system because the spectra of adsorbed NO exhibit prominent absorption bands, which appear at different frequencies, depending on whether the adsorption is on Mo or Co sites (11, 12, 21–26). Therefore, this technique can be used to determine whether one of the components is blocking the other. TPR, in combination with XPS and X-ray absorption spectroscopies can be used to determine the oxidation state of the components and to fully describe the structure of the catalyst after the different treatments. The use of a combination of techniques has been very successful in the study of sulfided Co : Mo catalysts, corroborating the CoMoS structure first proposed by Topsøe and co-workers (5, 7, 27–29). In this paper, we have used a combination of these techniques to put together a detailed picture of the structure of the catalyst, which can be used to explain the variations in selectivity toward SWNT observed when the catalyst formulations or pretreatment conditions are changed.

2. EXPERIMENTAL

2.1. Catalyst Preparation and Pretreatment

A series of mono and bimetallic Co-Mo catalysts supported on silica was prepared by incipient wetness impregnation. The bimetallic samples, prepared by coimpregnation of aqueous ammonium heptamolybdate and Co nitrate solutions, had Co : Mo molar ratios of 2 : 1, 3 : 4, 1 : 2, and 1 : 3. In this series, the amount of Mo was kept constant for all catalysts at 4.6 wt%, while the amount of Co was varied accordingly. Monometallic catalysts were prepared with loadings of 1.4 wt% Co and 4.6 wt% Mo, respectively. The SiO_2 support obtained from Aldrich had an average pore size of 6 nm, BET area of 480 m^2/g, pore volume of 0.75 cm^3/g, and particle sizes in the range 70–230 mesh. After impregnation, the solids were dried overnight at 120°C and then calcined for 3 h at 500°C in flowing dry air.

The catalysts were investigated in three different forms, the oxidic state, the reduced state, and after reaction. In the oxidic state, the catalysts were investigated directly after the calcination in air at 500°C. Those in the reduced state were first calcined in air at 500°C, then reduced step in H_2 flow for 1 h at 500°C, and finally heated in He flow to 700°C. This reduction/heating pretreatment is the one used here for the production of SWNT, which has proven to be the most effective (4).

2.2. Catalyst Characterization

The UV–vis spectra of the solid samples were recorded using a Shimadzu double beam spectrometer UV-2101 with an integrating sphere for diffuse reflectance. Barium sulfate was used as reflectance standard. Several Mo and Co compounds, including MoO_3, Na_2MoO_4, $(NH_4)_6Mo_7O_{24} \cdot 4H_2O$, and α-$CoMoO_4$, were used as references. Before each analysis, the samples were dried in air at 120°C.

The IR spectra of adsorbed NO were obtained on a Bio-Rad FTS 40 spectrometer, equipped with a diffuse reflectance cell (Harrick Scientific Co., Praying Mantis) with an *in situ* reaction chamber. Before the spectrum was acquired, the catalysts were reduced *ex situ* under H_2 flow at 500°C for 1 h and then heated in He to 700°C using a ramp temperature of 10°C/min. Then they were cooled to room temperature in He flow and transferred to the IR cell. To eliminate any superficial oxidation caused by exposure to air during the transfer, each sample was re-reduced *in situ* for 1 h at 500°C in H_2 flow, purged in He flow at that temperature, and then cooled to room temperature. Once cooled, the samples were exposed to 3% NO in He for 30 min at room temperature and purged in He for 30 min.

The X-ray absorption data were obtained at the National Synchrotron Light Source (NSLS) at Brookhaven National Laboratory, using beam line X-18B equipped with a Si(111) crystal monochromator. The X-ray ring at the NSLS has an energy of 2.5 GeV and ring current of 80–220 mA. The calcined, reduced, and spent samples were investigated by X-ray absorption. Both reduced and spent samples were not exposed to air but directly transferred from the reaction

chamber to a He glove bag, where they were wrapped in Kapton tape and stored in He-purged sealed veils until analysis. The EXAFS experiments were conducted in a stainless steel sample cell at liquid nitrogen temperature. Six scans were recorded for each sample. The average spectrum was obtained by adding the six scans. The pre-edge background was subtracted by using power series curves. Subsequently, the postedge background was removed using a cubic spline routine. The spectra were normalized by dividing by the height of the absorption edge. To obtain structural parameters, theoretical references for Co–Co, Co–O, Mo–O, Mo–C, Mo–Mo, and Co–Mo bonds were obtained by using the FEFF and FEFFIT fitting programs from the University of Washington (30–32). In this routine, the Debye–Waller factors for each bond type (σ), the edge energy difference (ΔE_o), the coordination number N, and the difference in bond distances (ΔR) with respect to the theoretical reference were used as fitting parameters. The quality of the fit was determined using the r-factor, which gives a sum-of-squares measure of the fractional misfit. Therefore, the smaller the r-factor, the better the fit is. For good fits, the r-factor is always less than or about 3%. The spectra of MoO_3, Na_2MoO_4, $(NH_4)_6Mo_7O_{24}$, Mo_2C, CoO, Co_3O_4, and α-$CoMoO_4$, as well as Co and Mo foils were also obtained at liquid nitrogen temperature and used as references.

XPS data were recorded on a Physical Electronics PHI 5800 ESCA System with monochromatic Al$K\alpha$ X rays (1486.6 eV) operated at 350 W and 15 kV with a background pressure of approximately 2.0×10^{-9} Torr. A 400-μm spot size and 58.7 eV pass energy were typically used for the analysis. Sample charging during the measurements was compensated for by an electron flood gun. The electron takeoff angle was 45° with respect to the sample surface. The pretreatment of the samples was performed in a packed bed reactor with an on/off valve at each end of the reactor, which allowed for a quick isolation of the samples after each treatment. The reactor with the sample under He was transferred to a glove bag; the sample (in powder form) was placed on a stainless steel holder and kept in a vacuum transfer vessel (model 04-110A from Physical Electronics) to avoid any exposure to the atmosphere before the analysis. For each sample, the binding energy regions corresponding to Si (95–115 eV), Mo (220–245 eV), and Co (760–820 eV) were scanned. The binding energies were corrected by reference to the C(1s) line at 284.8 eV. A nonlinear Shirley-type background was used for the area analysis of each peak. The fitting of the XPS spectra was carried out with asymmetric peaks, using the MultiPak software from Physical Electronics.

The H_2-TPR experiments were conducted passing a continuous flow of 5% H_2/Ar over approximately 30 mg of the calcined catalyst at a flow rate of 10 cm^3/min while linearly increasing the temperature at a heating rate of 8°C/min. The hydrogen uptake as a function of temperature was monitored using a thermal conductivity detector, SRI model 110 TCD.

2.3. Production and Characterization of Carbon Nanotubes

In this contribution, the production of SWNT by CO disproportionation is compared in a series of catalysts with Co : Mo ratios of 2 : 1, 1 : 2, and 1 : 3. A more extensive comparison has been done in a previous contribution (19). In the present work, we have selected catalysts that display contrasting behavior in selectivity. For the SWNT production, 0.5 g of calcined catalyst was placed in a horizontal tubular reactor, heated in H_2 flow to 500°C, and then in He flow to 700°C. Subsequently, CO was introduced at a flow rate of 850 cm^3/min at 84 psia and kept under these conditions for a given period of time, which ranged from 3 to 120 min. At the end of each run, the system was cooled in He flow. The total amount of carbon deposits was determined by temperature programmed oxidation (TPO) following the method described in our previous work (4). Transmission electron microscopy (TEM) and Raman spectroscopy were used for characterizing the carbon deposits on the catalyst. The TEM images were obtained in a JEOL JEM-2000FX TEM. For this analysis, a suspension of the carbon-containing samples in isopropanol was achieved by stirring the solid sample with ultrasound for 10 min. Then, a few drops of the resulting suspension were deposited on a grid and subsequently evacuated before the TEM analysis. The Raman spectra were obtained at Nicolet Instruments Corp., on a Nicolet Almega Dispersive Raman spectrometer with a 532 nm laser.

3. RESULTS

3.1. Characterization of the Calcined Catalysts

3.1.1. UV–vis DRS. We have used UV-vis-DRS to study the state of both Mo and Co in the oxidic form, after calcination in air at 500°C. In order to estimate the band energy gap of the Mo oxide compounds, Barnton *et al.* recommended using the square root of the Kubelka–Munk function multiplied by the photon energy, and plotting this new function versus the photon energy (33). The position of the absorption edge can then be determined by extrapolating the linear part of the rising curve to zero (20, 33). The values thus obtained carry information about the average domain size of the oxide nanoparticles. It has been shown that the energy band gap decreases as the domain size increases (20). Therefore, a comparison can be made between the energy of the samples under investigation and those of references of known domain size. This comparison is made in Fig. 1, which shows the absorption edges of several MoO_x species together with those of two different Co : Mo/SiO_2 catalysts. As expected, the band gap energies in the reference series decrease as the domain size

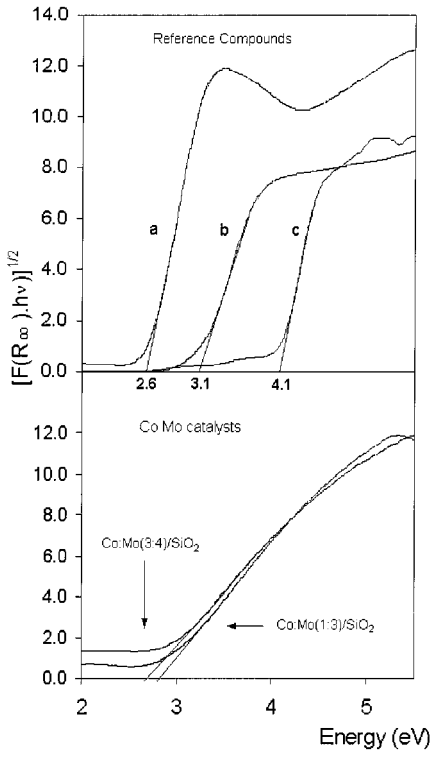

FIG. 1. Lower panel: UV absorption spectra for two Co : Mo/SiO_2 calcined catalysts. Upper panel: (a) MoO_3, (b) $(NH_4)_6Mo_7O_{24}$, (c) $NaMoO_4$ references.

increases. Those of the Co : Mo/SiO_2 catalysts lie between those of $(NH_4)_6Mo_7O_{24}$ and MoO_3. From this comparison, it can be inferred that the Mo species in the calcined catalysts have relatively small domain sizes. The presence of a small contribution of MoO_3 species could not be ruled out since a small tail can be observed below 3.0 eV, but most of the Mo is in a high state of dispersion.

In addition to the charge-transfer bands due to Mo appearing in the UV region, the visible spectra of the bimetallic catalysts present bands in the 500- to 750-nm region, which did not appear for the Mo/SiO_2 catalyst. These bands are associated with Co species and have previously been ascribed to d–d transitions ($^4T_{2g} \rightarrow {}^4A_{2g}$ and $^4T_{2g} \rightarrow {}^4T_{1g}(P)$) of high spin octahedral Co complexes (14). Figure 2 shows the DRS spectra in this region for three calcined catalysts, Co : Mo (3 : 4)/SiO_2, Co : Mo (1 : 3)/SiO_2, and Co/SiO_2. The spectrum for the Co : Mo (1 : 3) catalyst is very similar to that of α-$CoMoO_4$, which is typical of Co in an octahedral environment. The spectrum for the Co : Mo (1 : 2) was almost identical to that of the Co : Mo (1 : 3) catalyst, so only one of them is included in the graph. By contrast, the shape of the spectrum of the Co : Mo (3 : 4)/SiO_2 catalyst was markedly different and exhibited the appearance of a band at around 680 nm. This band was in turn the dominant feature in the pure Co catalyst and should be associated with Co_3O_4 species, which, as shown below, are present in the pure Co catalyst in the calcined state. Therefore, it can be concluded that the catalysts with low Co : Mo ratios exhibit most of the Co interacting with Mo. However, as the Co : Mo ratio increases, free Co oxide begins to appear. In fact, the spectrum of the Co : Mo (3 : 4)/SiO_2 catalyst can be rationalized as a sum of contributions from two types of species, one interacting with Mo (main band at around 600 nm) and a second one in which the Co oxidic species are segregated and not interacting with Mo (main band at 680 nm). Similar conclusions have been previously drawn from Raman spectroscopy and X-ray diffraction (XRD) data, which indicated that a noninteracting Co phase is formed on Co-Mo/SiO_2 catalysts at high Co : Mo ratios (17, 34).

3.1.2. EXAFS/XANES. Figure 3 shows the K-edges of Mo ($E = 20{,}000$ eV) for two different calcined catalysts with Co : Mo molar ratios of 2 : 1 and 1 : 3. Absorption spectra for the two reference compounds, α-$CoMoO_4$ and ammonium heptamolybdate, have been included for comparison. The absorption edges for both catalysts are remarkably similar. They both exhibit a pre-edge feature, which is also observed in the spectrum of ammonium heptamolybdate. This pre-edge feature is typically observed in distorted octahedral environments, such as that found in the heptamolybdate. It is due to a 1s $\rightarrow$ 4d bound-state transition that in the case of a perfect octahedral geometry is formally forbidden. Accordingly, it is barely present in compounds such as MoO_3 and α-$CoMoO_4$. However, it becomes allowed when the d-states of the metal mix with the *p* orbitals of

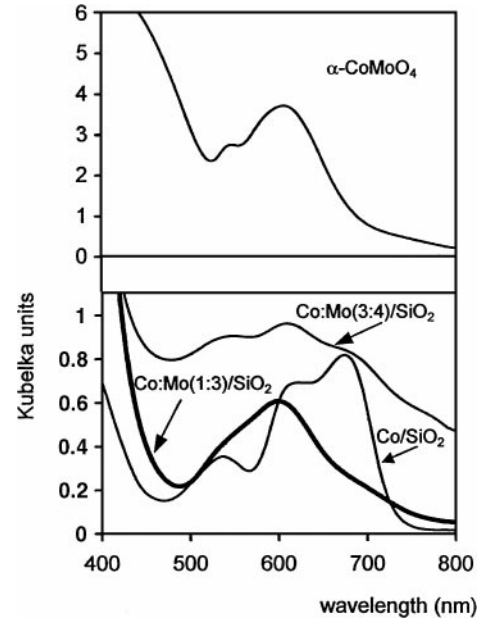

FIG. 2. Visible spectra for two calcined bimetallic Co : Mo/SiO_2 catalysts with different Co : Mo ratios (1 : 3 and 3 : 4) and that for a monometallic Co (0.02 wt%)/SiO_2. The spectrum of an α-$CoMoO_4$ reference is included for comparison.

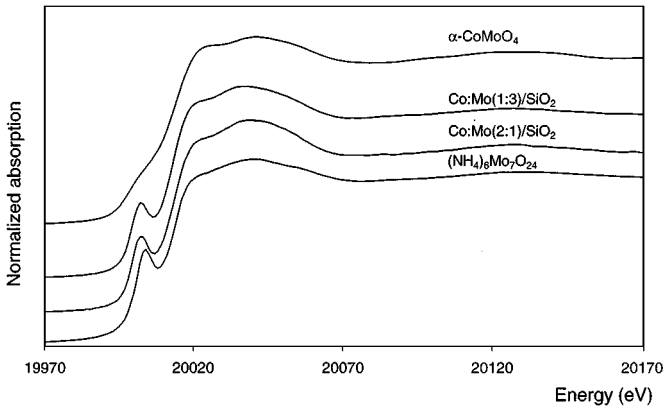

FIG. 3. Mo-edge (20,000 eV) XANES of two CoMo calcined catalyst compared to α-$CoMoO_4$ and $(NH_4)_6Mo_7O_{24}$ references.

the ligand, as in compounds with distorted octahedral symmetries (19, 35, 36). Of course, a pre-edge feature is always observed in Mo species with tetrahedral symmetry, such as in Na molybdate. However, in such cases the feature is much more pronounced than that observed here. Therefore, it can be concluded that in the bimetallic catalysts, Mo is mostly in a structure similar to that of the heptamolybdate. It is interesting that this is the same for both the Co : Mo (2 : 1) and Co : Mo (1 : 3) samples.

Next, it is important to investigate the same set of samples at the Co edge. Figure 4 compares the XANES spectra for the K-edge of Co (E_o = 7709 eV) in the calcined Co : Mo (1 : 3)/SiO_2 catalyst and that in the α-$CoMoO_4$ reference. Except for some difference in the size and shape of the first peak in the edge, both spectra look remarkably similar. By contrast, the Co edge for the Co : Mo (2 : 1) catalyst, containing excess Co, is very different from that of the α-$CoMoO_4$ reference. As shown in Fig. 5A, the XANES of the catalyst is in fact very similar to that of Co_3O_4, although a small shoulder appearing at around 7726 eV is more pronounced for the catalyst than for the oxide. It is interesting to note

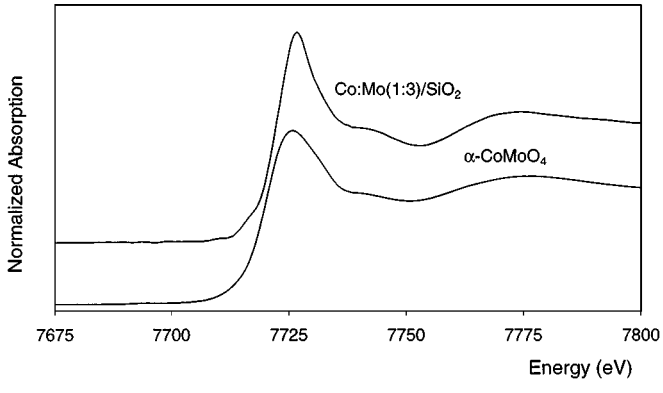

FIG. 4. Co K-edge (7719 eV) XANES of calcined Co : Mo (1 : 3)/SiO_2 catalyst compared to α-$CoMoO_4$ used as a reference.

that this shoulder coincides with the white line of $CoMoO_4$ and CoO species. A first approximation of a XANES composed of two different phases can be obtained by simple addition of the XANES of the individual components. A simple fitting with a linear combination of contributions from Co_3O_4 and $CoMoO_4$ reproduces the XANES spectrum of the Co : Mo (2 : 1) catalyst (see Fig. 5B). This comparison indicates that in the catalyst with Co excess, most of the Co is in the form of Co_3O_4 and a small fraction is $CoMoO_4$. When the fitting was attempted using CoO as a third component, the best fit did not include any contribution of this oxide. The EXAFS data were in good agreement with the conclusions reached from the XANES analysis. As shown, in Fig. 6, the Fourier transform for the calcined Co : Mo (2 : 1) catalyst is very similar to that of Co_3O_4, indicating that this oxide is the predominant form present when Co is in excess.

The results on the sample with low Co : Mo ratio require some further consideration. It is interesting to note that while the XANES spectra for these catalysts look similar to that of α-$CoMoO_4$ from the Co side, they bear no

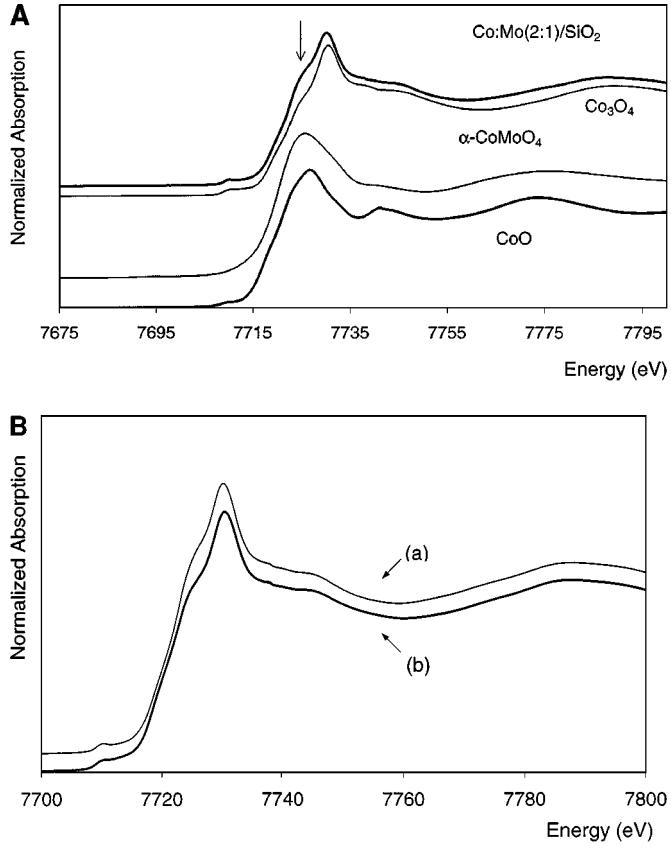

FIG. 5. (A) Co K-edge XANES of a calcined Co : Mo (2 : 1)/SiO_2 catalyst compared to those of α-$CoMoO_4$, CoO, and Co_3O_4 references. (B) Co K-edge XANES of a calcined Co : Mo (2 : 1)/SiO_2 catalyst (curve a) and a weighted linear combination of XANES from α-$CoMoO_4$ and Co_3O_4 (curve b). The contributions resulting from the best fit were 82% Co_3O_4 and 18% α-$CoMoO_4$.

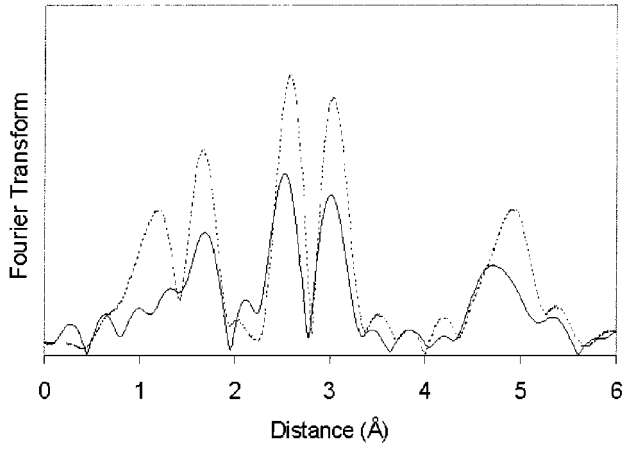

FIG. 6. Fourier transforms of the k^3 EXAFS data of the Co K-edge obtained on the calcined Co : Mo (2 : 1)/SiO_2 catalyst (solid line) and for Co_3O_4 reference (dotted line).

resemblance to this compound from the Mo side. One may rationalize this contrasting behavior by proposing that while most of the Co in the catalyst is forming a $CoMoO_4$-like phase, only a fraction of Mo participates in this compound. The rest of the Mo would be in a dispersed Mo oxide. We propose that the Co is in a $CoMoO_4$-like phase because the XANES indicates that the local environment of Co in the Co : Mo (1 : 3) catalyst is very similar to that in $CoMoO_4$, but the EXAFS data are significantly different from that of the compound. This comparison is made in Fig. 7, which shows the Fourier transforms for the K-edge of Co in the calcined Co : Mo (1 : 3)/SiO_2 catalyst, together with that of α-$CoMoO_4$. The low intensity observed in the catalyst for the peaks between 2.5 and 4 Å, clearly observable for the Co molybdate, would indicate that bulk α-$CoMoO_4$ is not present, but rather a highly dispersed $CoMoO_4$-like structure, coexisting with Mo oxide species.

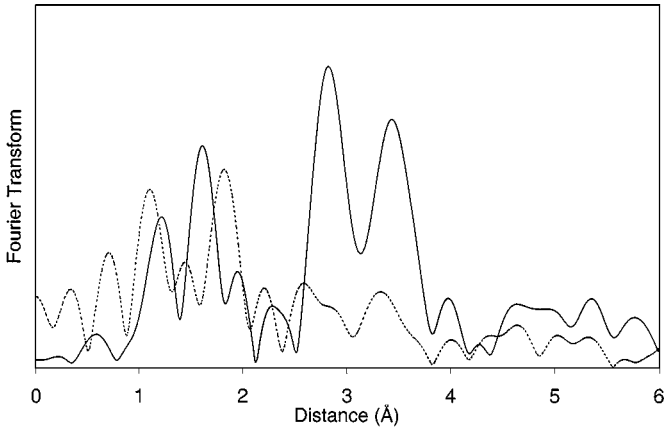

FIG. 7. Fourier transforms of the k^3 EXAFS data of the Co K-edge, obtained on the calcined Co : Mo (1 : 3)/SiO_2 catalyst (dotted line) and on a α-$CoMoO_4$ reference (solid line).

3.1.3. TPR. The reduction profiles of calcined monometallic Co/SiO_2 and Mo/SiO_2 catalysts together with that of the bimetallic Co : Mo (1 : 3)/SiO_2 catalyst are shown in Fig. 8a. The TPR profile of the Co monometallic catalyst shows two peaks at 360 and 445°C, which can be ascribed to the reduction of Co oxide species. The reduction of the monometallic Mo catalyst also exhibits two peaks, but they appear at much higher temperatures than those of Co. Therefore, from the reduction profiles it is possible to identify the presence of Co and Mo species in the absence of interactions. Accordingly, the TPR of the bimetallic Co : Mo (1 : 3)/SiO_2 catalyst indicates that in this sample, the vast majority of Co oxide species are interacting with Mo. It is clear that while most of the Co in the monometallic catalyst gets reduced below 500°C, almost no reduction takes place below that temperature in the bimetallic catalyst. It has been reported that the reduction of interacting Co–Mo-supported species occurs at similar temperatures as those assigned for the reduction of free Mo species (17). It has also been proposed that the addition of Mo oxide to Co oxide inhibits the reduction of the Co species because Mo^{6+}

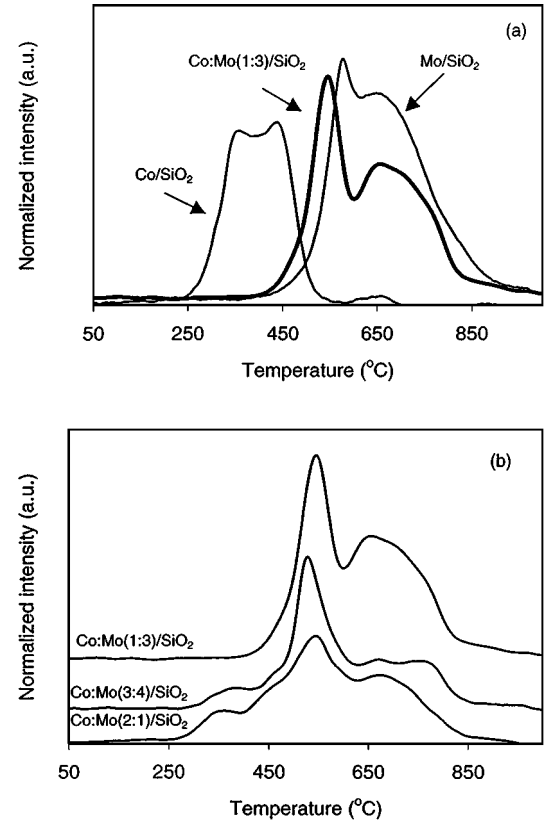

FIG. 8. (a) TPR profiles of monometallic Co/SiO_2 and Mo/SiO_2 catalysts compared to the Co : Mo (1 : 3)/SiO_2 bimetallic catalyst. (b) TPR profiles of Co-Mo/SiO_2 bimetallic catalysts with varying Co : Mo ratios. In all cases the reduction was conducted under 5% H_2/Ar, using a heating linear ramp of 8°C/min.

polarizes the Co–O bonds, making them more ionic and consequently more difficult to reduce (37). In agreement with the DRS and EXAFS/XANES data, TPR indicates that a high degree of Co-Mo interaction is only observed for the catalyst with a low Co : Mo ratio. As shown in Fig. 8b, as the Co : Mo ratio increases, a gradually increasing fraction of segregated Co species is apparent from the peaks at 360 and 445°C, which are associated with the reduction of noninteracting Co oxide.

3.2. Characterization of the Reduced Catalysts

3.2.1. DRIFTS. The vibrational spectrum of adsorbed NO was used to investigate the Co : Mo/SiO_2 catalysts after the reduction pretreatment in H_2 at 500° C. As mentioned above, both Co and Mo are able to adsorb NO at room temperature, exhibiting characteristic IR absorption bands that can be used to identify the NO adsorption on each metal. It is generally agreed that Mo^{VI} does not adsorb NO (22), but Mo^{II}, Mo^{III}, and Mo^{IV} have all been suggested as potential NO adsorption sites (11, 24). Similarly, both calcined and reduced Co catalysts are able to adsorb NO (26). It has been reported that adsorption on reduced Co results in bands at slightly lower frequencies than on oxidized Co (25). However, it is not always possible to determine the chemical state of Co based on NO adsorption. Therefore, although DRIFTS of adsorbed NO may not be the best technique to characterize the chemical state of Co and Mo, it is certainly a powerful tool to quantify the degree of site blocking of one of the two components by the other.

Figure 9 shows the DRIFTS spectrum of NO adsorbed on two monometallic catalysts with 4.6 wt% Mo and 1.4 wt% Co, and a bimetallic catalyst with 4.6 wt% Mo and 1.4 wt% Co (Co : Mo = 1 : 2). On the monometallic Mo/SiO_2 catalyst, the bands corresponding to the symmetric and antisymmetric stretching modes of dinitrosyl species are clearly observed. The symmetric mode exhibited a band at 1814 cm^{-1}, while the antisymmetric mode generated a broad band centered at around 1714 cm^{-1}. Yao and Rothschild (23) have attributed the broadening of the antisymmetric band to inhomogeneities on the surface that influence the vibrational transition moment of the asymmetric mode more than the moment of the symmetric mode. For the monometallic Co/SiO_2 catalyst, the bands of the dinitrosyl species appeared at significantly higher wavenumbers (1880 and 1803 cm^{-1}) than those on Mo. In this case, the antisymmetric mode is the dominant band in the spectrum. Finally, the bimetallic Co : Mo (1 : 2)/SiO_2 catalyst showed three absorption bands that roughly correspond to those of the individual components. The dominant band appearing at 1806 cm^{-1} obviously has contributions from both the symmetric band of NO adsorbed on Mo and the antisymmetric band of NO adsorbed on Co. A smaller band appeared at 1883 cm^{-1}, which can be associated with the symmetric mode on Co sites, and a broader

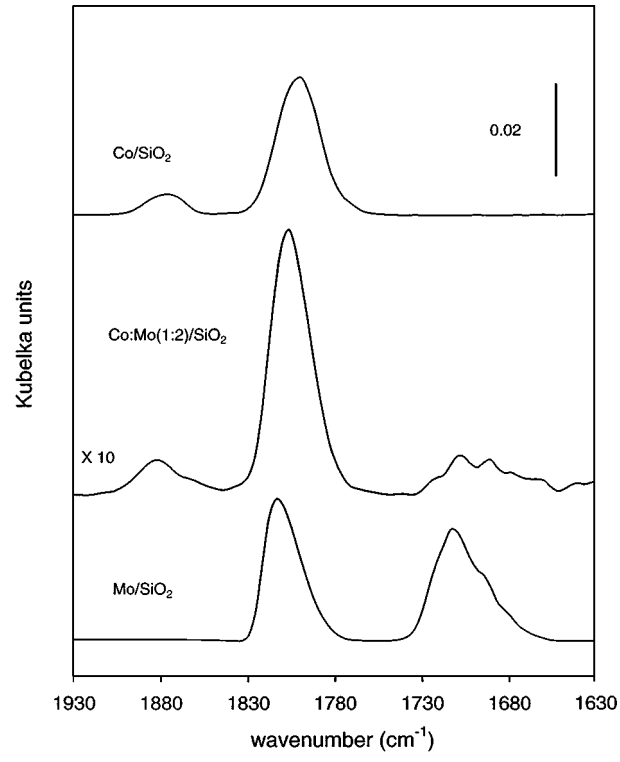

FIG. 9. IR spectra of NO adsorbed on monometallic (Mo/SiO_2 and Co/SiO_2) and bimetallic (Co : Mo/SiO_2) catalysts. The catalysts were reduced under hydrogen at 500°C.

band, which may include several individual bands, appeared in the region of 1730–1650 cm^{-1} and can only be associated with adsorption on Mo. The appearance of different components associated with this asymmetric-mode band in the bimetallic catalyst contrasting to that on Mo/SiO_2 catalyst could be explained in terms of Mo sites with different degrees of coordinative unsaturation (12), or alternatively, in terms of sites where Mo is influenced by Co to various degrees. It is also interesting to note that the overall intensity of the bands of the bimetallic Co-Mo catalysts is consistently much lower than that of the monometallic Co and Mo catalyst. This effect has been previously observed for alumina-supported Co-Mo catalysts. In that case, a lower dispersion of the active species on the bimetallic catalysts, compared to that of the monometallic ones, was considered responsible for the observed loss in intensity (22).

Figure 10 shows the Fourier transform infrared (FTIR) spectra of NO adsorbed on different reduced bimetallic catalysts, in which the Mo content was kept constant while the Co content was increased. It is clear that as the Co content increases, the adsorption of NO over the Mo sites is inhibited. A similar effect has been previously reported for the sulfided Co : Mo/Al_2O_3 catalyst and interpreted as a blockage of Mo sites by Co (21). Since the low-frequency antisymmetric NO stretching on Mo does not have contributions from species adsorbed on Co, it can be used as

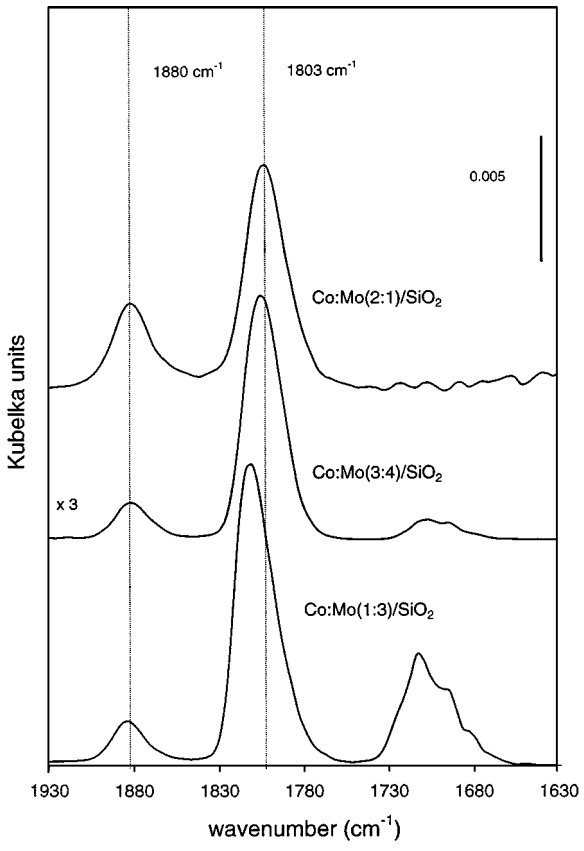

FIG. 10. IR bands of NO adsorbed on Co : Mo (2 : 1)/SiO_2, Co : Mo (3 : 4)/SiO_2, and Co : Mo (1 : 3)/SiO_2. The catalysts were reduced under hydrogen at 500°C.

an indication of the density of Mo sites covered by Co. A clear decrease in the intensity of this band is observed as the Co : Mo ratio increases, becoming practically negligible when Co is in excess (e.g., for a Co : Mo ratio of 2 : 1). At the same time, the bands for this catalyst appear at the same wavelengths as those on the monometallic Co catalyst (i.e., 1880 and 1803 cm^{-1}). A straightforward conclusion drawn from these observations is that when Co is in excess, it almost completely covers the Mo sites, while the excess Co forms a noninteracting species.

3.2.2. XPS. XPS can be used to determine the chemical nature of the catalyst constituents and to roughly estimate their distribution on the surface. For the first purpose, the binding energy of the catalysts can be compared to those of reference compounds. In Table 1, the binding energies of the Co $2p_{3/2}$ and Mo $3d_{5/2}$ levels obtained for the catalysts in the reduced state are compared to those of the reference compounds. The spectra corresponding to the Co $2p_{3/2}$ levels for all the catalysts can be described in terms of two contributions, one appearing at about 778 eV and other at 781.5 eV. As shown in the table, these binding energies are in good correspondence with the binding energies that were obtained for the metallic Co (778.2 eV) and the $CoMoO_4$ (781.4 eV) references, respectively. Similar values for these reference materials have been previously reported in the literature (14, 26, 37, 38). The respective surface fractions of Co in the two chemical states were obtained by fitting the spectra with asymmetric curves centered at the corresponding binding energies. The fraction of Co in the metallic state after reduction at 500°C, as determined from this analysis, is shown in Fig. 11 as a function of the Co : Mo ratio. At low

TABLE 1

Binding Energies for Reduced Catalysts and Reference Compounds

Determinant	Binding energies (eV) Mo $3d_{5/2}$	Co $2p_{3/2}$
Reference Samples		
Co		778.2
CoO		780.5
Co_3O_4		780.1
α-$CoMoO_4$	232.5	781.4
MoO_3	232.4	
MoO_2	229.1	
$(NH_4)_6Mo_7O_{24} \cdot 4H_2O$	232.3	
Reduced Catalysts		
Mo/SiO_2	229.2	
	231.0	
	233.4	
Co : Mo (1 : 3)/SiO_2	228.9	778.1
	231.1	781.5
	233.9	
Co : Mo (1 : 2)/SiO_2	228.3	777.9
	230.8	780.7
	233.3	
Co : Mo (3 : 4)/SiO_2	228.9	778.5
	230.8	781.5
	233.1	
Co : Mo (2 : 1)/SiO_2	228.7	778.4
	230.9	781.4
	233.2	

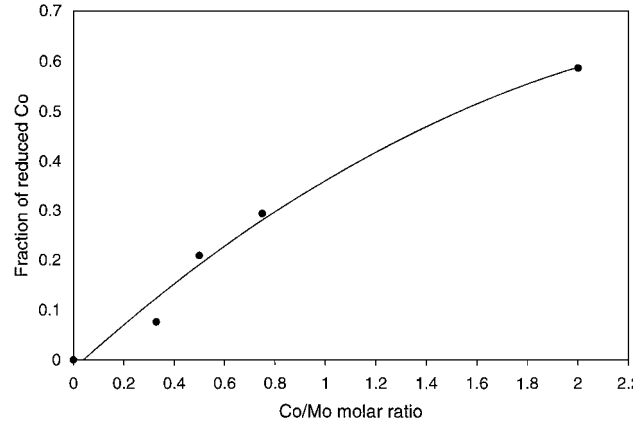

FIG. 11. Fraction of cobalt reduced to the metallic state as a function of Co : Mo nominal ratio, as determined by XPS on samples pretreated under H_2 at 500°C and heated in He at 700°C, without exposure to air.

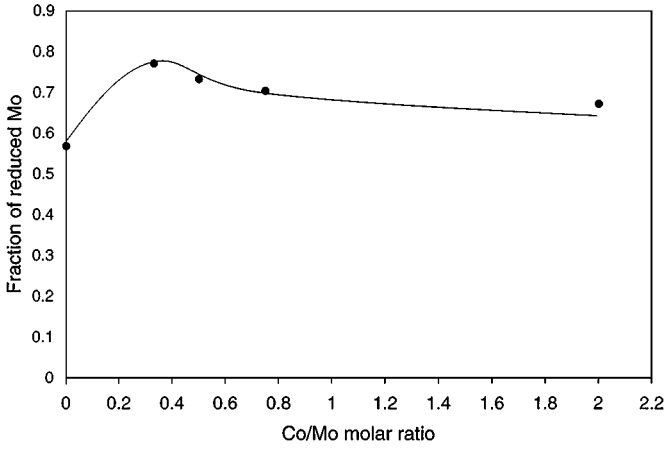

FIG. 12. Fraction of reduced Mo (i.e., Mo^{4+} + Mo^{5+}) as a function of Co : Mo nominal ratio, as determined by XPS on samples pretreated under H_2 at 500°C and heated in He at 700°C, without exposure to air.

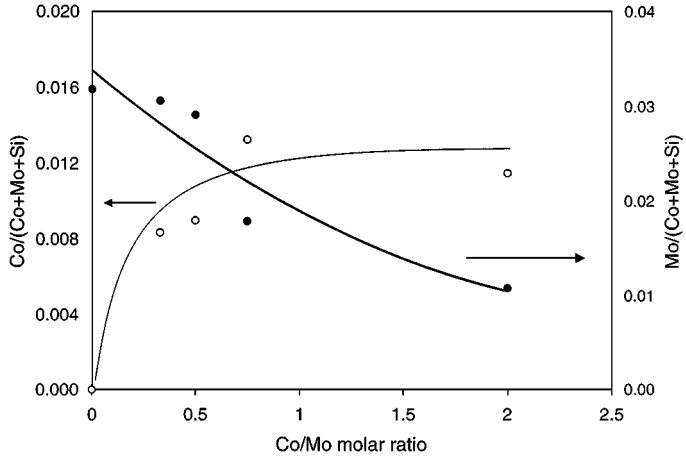

FIG. 13. Surface atomic percentage of molybdenum (filled circles) and cobalt (open circles) as function of the nominal Co : Mo ratio, as determined by XPS on samples pretreated under H_2 at 500°C and heated in He at 700°C, without exposure to air.

Co : Mo ratios, when the majority of the Co oxide species are interacting with Mo, most of the Co remains in the oxidic form, but as the Co : Mo ratio increases, a larger fraction of Co gets reduced. In agreement with this trend and with the TPR data shown above, previous reports have indicated that the Co–Mo interacting phase is, in fact, more difficult to reduce than Co oxide alone (17).

The assignment of the Mo $3d_{5/2}$ levels to different chemical states of Mo is not as straightforward as that of Co. As shown in Table 1, the spectra of the reduced catalysts can be described in terms of three contributing peaks. The one at the lowest binding energy appears in the same region as that of Mo^{4+} in MoO_2. The one at the highest binding energy (233.1–233.9 eV) appears at slightly higher energy than that of Mo^{6+} in MoO_3. This peak has been previously assigned to Mo^{6+} species in an oxidic environment (37, 39), although some authors have indicated that these species should have binding energies in the region of 232.5–232.7 eV (40, 41). The remaining peak appearing at around 231 eV can be attributed to Mo in an intermediate state such as Mo^{+5}, as previously proposed (37, 42). From the fitting of the spectra of the different catalysts with asymmetric curves centered at the indicated binding energies, the fraction of reduced Mo (i.e., Mo^{4+} + Mo^{5+}) has been calculated and plotted in Fig. 12 as a function of the Co : Mo ratio. It is observed that except for the monometallic catalyst, there is a slight decrease on the reducibility of Mo as the Co : Mo ratio increases. That is, the Co-Mo interaction is also evident from the Mo analysis, although the effect is not as pronounced as for Co.

In Table 2, we report the surface atomic fractions of Co and Mo on the catalyst after the reduction pretreatment. The intensity of the Si peak remained almost constant for all samples, except for the catalyst with a Co : Mo ratio of 2 : 1, in which it decreased. Figure 13 shows the fractions of Co/Si and Mo/Si as a function of bulk Co : Mo ratio. It is seen that even though the Mo concentration in the catalyst was kept constant, the Mo/Si ratio clearly decreased as the amount of Co increased. In agreement with the DRIFTS

TABLE 2

Surface Atomic Concentrations for Reduced Catalysts as Determined by XPS

	Atomic concentration (%)		
Reduced catalysts	Mo	Co	Si
Mo/SiO_2	1	0	30.41
Co : Mo (1 : 3)/SiO_2	0.99	0.27	31.08
Co : Mo (1 : 2)/SiO_2	0.94	0.29	31.04
Co : Mo (3 : 4)/SiO_2	0.58	0.43	31.42
Co : Mo (2 : 1)/SiO_2	0.33	0.35	29.77

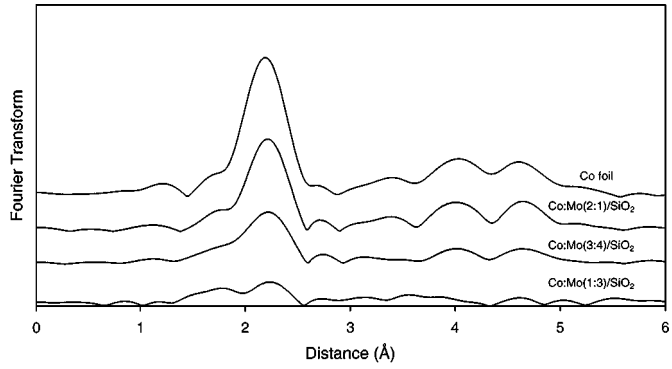

FIG. 14. Fourier transforms of the k^3 EXAFS data of the Co K-edge obtained for several Co : Mo/SiO_2 reduced catalysts with different Co/Mo ratios. The data for a Co foil are included for comparison.

TABLE 3

Structural Parameters Resulting from the Fitting of the Co-Edge EXAFS Data Obtained for the Co : Mo (2 : 1)/SiO_2 Catalyst

	Fitting ($E_0 = 8.2$)				
Reference phase	Bond	Coordination number	Distances	Sigma	*r*-factor
Co°	Co–Co (first shell)	7.8	2.492	0.0046	0.0014
	Co–Co (second shell)	2.4	3.523	0.0047	
	Co–Co (third shell)	9.6	4.327	0.0059	

Note. E_0 represents the energy shift, sigma is the Debye–Waller factor, and the *r*-factor is a measurement of the fit quality.

data, these results show that the addition of Co results in a gradual coverage of Mo.

3.2.3. EXAFS. The EXAFS results for the reduced catalysts, shown in Fig. 14, reveal a definite trend, which ties in nicely with the XPS data. The data indicates that, keeping the amount of Mo fixed, the fraction of metallic Co increases with the Co : Mo ratio. The appearance of clearly observable peaks in the range corresponding to the second and thrid coordination spheres (0.25–0.45 nm) indicates that larger Co° clusters are present on the catalyst with the higher Co content. To quantify this trend, the data for the first, second, and third coordination shells of Co on the Co : Mo (2 : 1)/SiO_2 were isolated by applying an inverse Fourier transform over a restricted range of *r* (0.13–0.45 nm). The filtered data were then fitted using the FEFFIT program and assuming that only Co° was present. As shown in Fig. 15, the quality of this fit was excellent. The structural parameters resulting from the fit are summarized in Table 3. From the above results, we can conclude that in the reduced Co : Mo/SiO_2 with high Co : Mo ratios, a large fraction of Co is in the form of metallic Co clusters.

To compare the structures of the Co phases in the catalysts with low Co : Mo ratios with those of high Co : Mo ratios, filtered EXAFS data were fitted for the Co : Mo (1 : 3) catalyst, as previously described. In the first attempt, the EXAFS data were fitted using a single phase, which was either metallic or oxidized Co. In both cases, the results were unsatisfactory. A more complex model was needed to obtain a good fit. In the second model used for fitting, the simultaneous presence of metallic Co clusters and oxidized Co species was considered. Satisfactory fits were only obtained with the simultaneous presence of Co metallic clusters and a $CoMoO_4$ phase. Figure 16 illustrates the quality of the fit, while Table 4 summarizes the structural parameters determined from the analysis. The resulting parameters indicate that in this catalyst, cobalt is mainly forming a $CoMoO_4$-like phase and a small fraction is forming metallic Co.

3.3. Production of Carbon Nanotubes by Catalytic Disproportionation of CO

The ability of the different catalysts to produce SWNT by CO disproportionation was tested by passing pure CO over the catalyst at 700°C. Before the reaction, the catalysts were calcined in air at 500°C, then reduced in H_2 at 500°C, and then heated in He flow to the reaction temperature. At the

TABLE 4

Structural Parameters Resulting from the Fitting of the Co-Edge EXAFS Data Obtained for the Co : Mo (1 : 3)/SiO_2 Catalyst

	Fitting ($E_0 = 9.88$)				
Phase	Bond	Coordination number	Distances (Å)	Sigma	*r*-factor
α-$CoMoO_4$	Co–O (first shell)	3	2.1 ± 0.18	0.0029	0.0323
	Co–Co (first shell) &	1	3.03	0.0035	
	Co–Mo (first shell)		3.15		
	Co–O (second shell)	3	3.7 ± 0.05	0.0019	
	Co–Mo (second shell)	3.2	3.9 ± 0.13	0.0027	
Co°	Co–Co (first shell)	1.5	2.50	0.0035	
	Co–Co (second shell)	2.2	3.65	0.0023	
	Co–Co (third shell)	1.6	4.35	0.0033	

Note. Six different scattering paths were used for the Co–O (first and second shells) and Co–Mo (second shell) pairs.

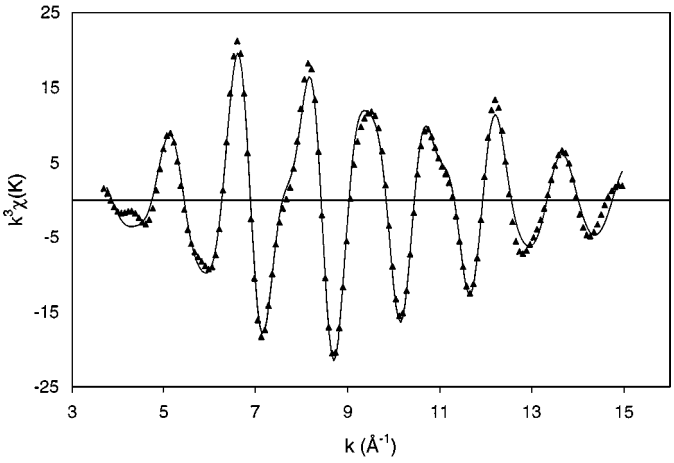

FIG. 15. Fit in *k*-space for Co : Mo (2 : 1)/SiO_2. Experimental (triangles) and modeled EXAFS contribution around Co (full line).

end of a 2-h reaction period, the spent catalyst containing the carbon deposits was cooled in He flow. The characterization of the carbon deposits was done using three main techniques that we have previously used and tested. They are temperature programmed oxidation (TPO), transmission electron microscopy (TEM), and Raman spectroscopy. We have previously shown that from the TPO results we can obtain a quantitative measure of the carbon yield and selectivity toward SWNT (4). These results are summarized in Table 5 and illustrate the strong influence of the Co : Mo ratio on SWNT selectivity. The TEM observations totally support the TPO results. As shown in Figs. 17 and 18, a contrasting difference is observed in the carbon structures produced with the two different samples. While the sample with a Co : Mo ratio of 1 : 3 exhibited a high density of SWNT, the sample with a Co : Mo ratio of 2 : 1 mainly produced multiwalled carbon nanotubes (MWNT) and graphitic carbon deposits. In the first case, one can observe the typical parallel lattice fringes characteristic of SWNT. In the second case, a spacing of 0.34 nm can be observed between the fringes, which is characteristic of the space between individual walls in MWNT (43).

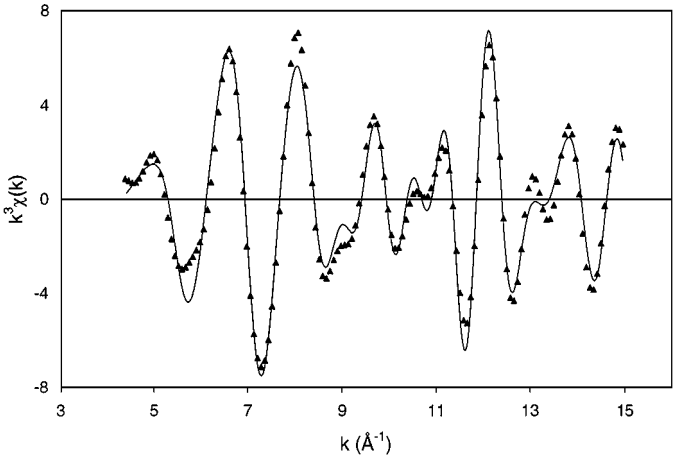

FIG. 16. Fit in *k*-space for Co : Mo (1 : 3)/SiO_2. Experimental (triangles) and modeled EXAFS contribution around Co (full line).

TABLE 5

Carbon Yield and Selectivity for Two Catalysts with Different Co : Mo Ratios

Catalysts	Amorphus carbon (%)	SWNT (%)	MWNT and graphite (%)	Total carbon yield (%)
Co : Mo (1 : 3)/SiO_2	18.7	70.7	10.6	18.25
Co : Mo (2 : 1)/SiO_2	14.8	15.2	70.0	16.35

Note. The yield is defined as mass of total deposited carbon per mass of catalyst. The selectivity to SWNT is the mass of SWNT per total mass of carbon deposits.

Raman spectroscopy provides valuable information about the structure of carbon nanotubes. The analysis of the radial A_{1g} breathing mode (below 300 cm^{-1}) gives direct information about the tubes diameter, while the analysis

FIG. 17. TEM images showing SWNT produced by CO disproportionation on a Co : Mo (1 : 3)/SiO_2 catalyst.

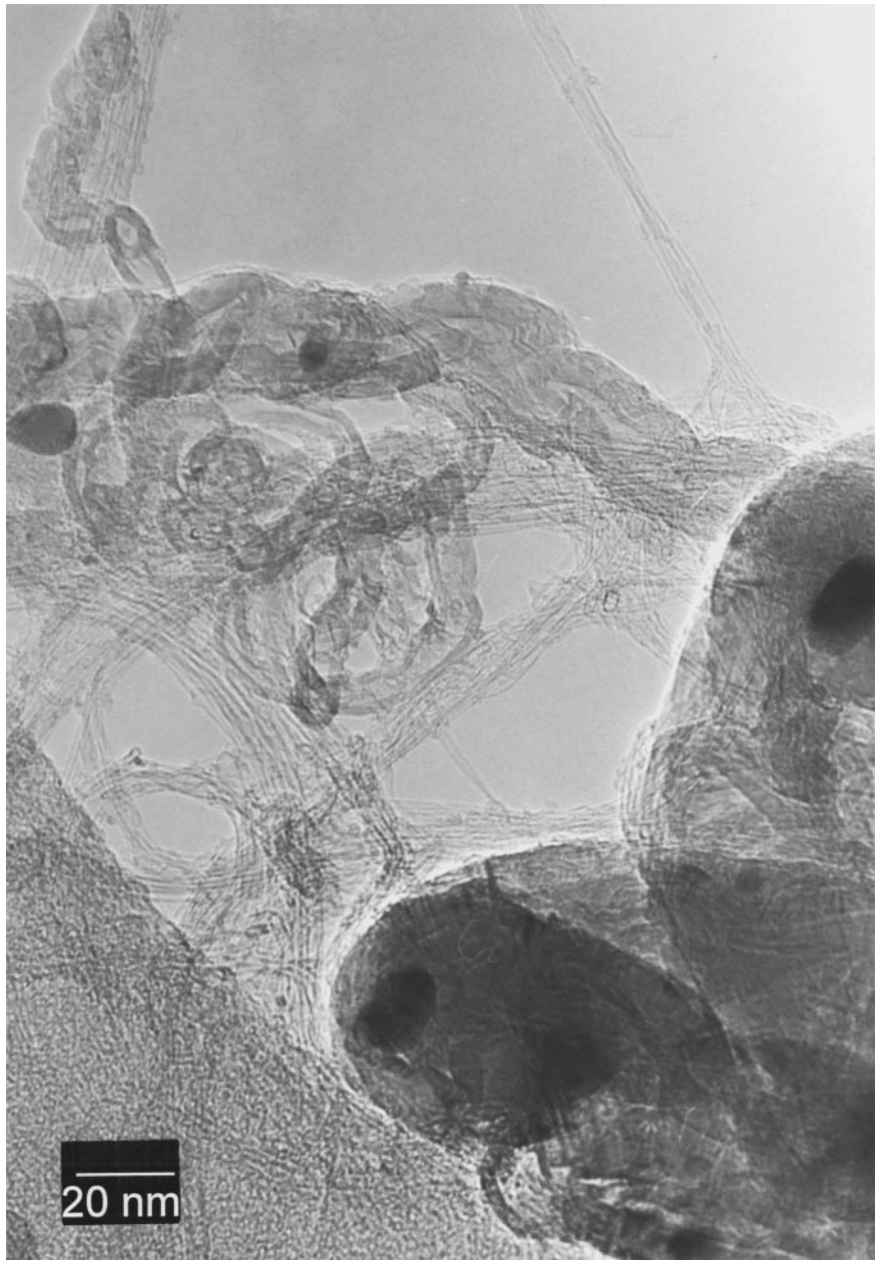

FIG. 18. TEM images showing a mixture of SWNT, MWNT, and graphite produced by CO disproportionation on a Co : Mo (2 : 1)/SiO_2 catalyst.

of the tangential mode (TM) range (i.e., 1400–1700 cm^{-1}) provides information on the electronic properties of the tubes. In addition, the analysis of the so-called D band at around 1350 cm^{-1} gives an indication of the level of disordered carbon. The size of the D band relative to the TM band at around 1590 cm^{-1}has been used as qualitative measurement of the formation of undesirable forms of carbon (44, 45). Figure 19 shows the Raman spectrum obtained with an excitation source of 532 nm on the carbon deposits formed on the catalyst with a low Co : Mo ratio. In agreement with the TPO and TEM results, the spectrum shows a high selectivity toward SWNT and a dominant band in the breathing mode region, centered at 265 cm^{-1}. A nonlinear relationship has been recently developed, by which the diameter of a tube in a bundle is directly given by the expression $\nu(cm^{-1}) = 238/(d(nm))^{0.93}$ (46). Accordingly, the band observed at around 265 cm^{-1} would correspond to a tube diameter of 0.89 nm.

It is noteworthy mentioning that when the Co : Mo (1 : 3)/SiO_2 catalyst that exhibited a high yield and selectivity toward SWNT was employed without the reduction step or with an exceedingly high reduction temperature,

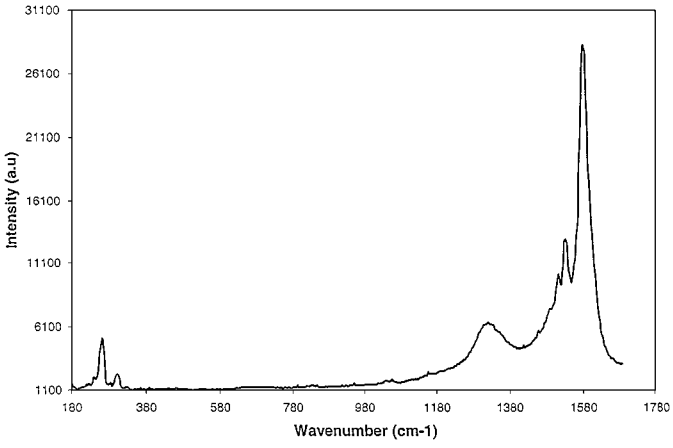

FIG. 19. Raman spectrum of the carbon nanotubes produced by catalytic disproportionation of CO on Co : Mo (1 : 3)/SiO_2 at 700°C. Excitation laser energy at 532 nm.

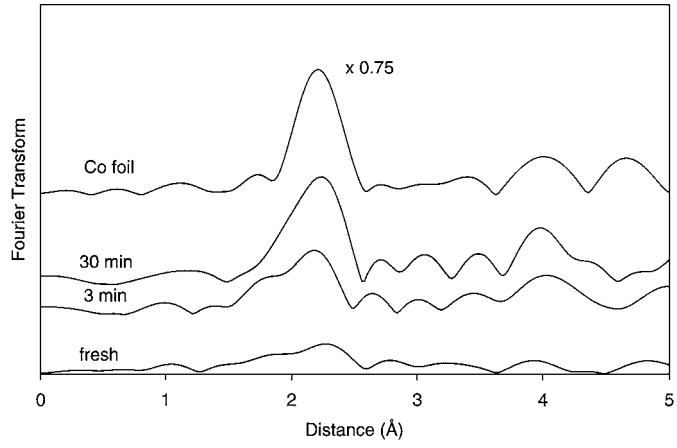

FIG. 20. Fourier transforms of the k^3EXAFS data obtained for the K-edge of Co for a fresh Co : Mo (1 : 2)/SiO_2 catalyst reduced in hydrogen (500°C), and after the growth of carbon nanotubes for reaction periods of 3 and 30 min. The EXAFS data of a Co foil are included for comparison.

poor SWNT yields were attained. It is suggestive that the TPR indicates that the Co reduction in the Co : Mo (1 : 3) does not start below 500°C. One may surmise that some degree of reduction, perhaps creation of oxygen vacancies around Mo, is necessary, since a totally oxidized catalyst is not efficient. On the other hand, a high degree of reduction of the catalyst, causing the appearance of metallic Co, is also detrimental for selectivity toward SWNT.

3.4. Characterization of the Spent Catalysts

The EXAFS results for the spent catalysts are shown in Fig. 20. The Fourier transform of the EXAFS data for the K-edge of Co ($E_o = 7709$ eV) for the Co : Mo (1 : 2) catalyst shows that after the pretreatment and before the reaction with CO, a significant fraction of Co remains oxidized. However, as the reaction proceeds, metallic Co begins to form, and after 30 min, the Fourier transform is indicative of pure Co metal. Undoubtedly, during the formation of carbon nanotubes over the selective catalyst, Co is gradually reduced to the metallic state. The detailed structural analysis of the Co EXAFS data indicated that as the reaction proceeds, the Co reduction is accompanied by an increase in metal particle size. Evidence for this process is presented in Table 6, where an increase in the Co–Co coordination number as a function of reaction time is observed.

In the same way, as illustrated in Fig. 21, after a 30-min reaction period, the Fourier transforms of the EXAFS data of Mo ($E_o = 20{,}000$ eV) reveal a drastic change, developing peaks that correspond exactly to those of the Mo_2C reference. The transformation of oxidized Mo species into Mo carbide during the reaction is indeed very clear, with a small fraction of unconverted Mo oxide remaining in the catalyst. This conversion can be clearly seen from the EXAFS

TABLE 6

Structural Parameters for the Co : Mo (1 : 2)/SiO_2 Catalyst after Different Reaction Periods, as Obtained from the EXAFS Data Analysis

Sample	Sample treatment	Edge (M)	E_0	Sigma	Coordination			Distances (Å)	r-factor
					N_{M-M}	N_{M-O}	N_{M-C}		
Co : Mo (1 : 2)/SiO_2	Spent 3 min	Co	4.2	0.0068	5.8	—	—	2.47	0.043
				0.0025	—	2.2	—	2.05	
Co : Mo (1 : 2)/SiO_2	Spent 30 min	Co	9.4	0.0065	9.2	—	—	2.50	0.020
				0.0003	—	1.1	—	2.07	
Mo_2C	Reference	Mo	6.6	0.0063	11.6	—	—	2.97	0.022
				0.0106	—		5.8	2.08	
Co : Mo (1 : 2)/SiO_2	Spent 30 min	Mo	7.1	0.0075	6.7	—	—	2.98	0.038
				0.0075	—	0.9	—	2.09	
				0.0039	—	—	3.3	1.68	

Note. E_0 represents the energy shift; σ is the Debye–Waller factor; N_{M-M}, N_{M-C}, and N_{M-O} are the coordination numbers between the metals (Mo or Co) with another metal atom, a C atom, and an O atom, respectively; R (Å) is the coordination distance for each respective bond; and the r-factor is a measurement of the fit quality.

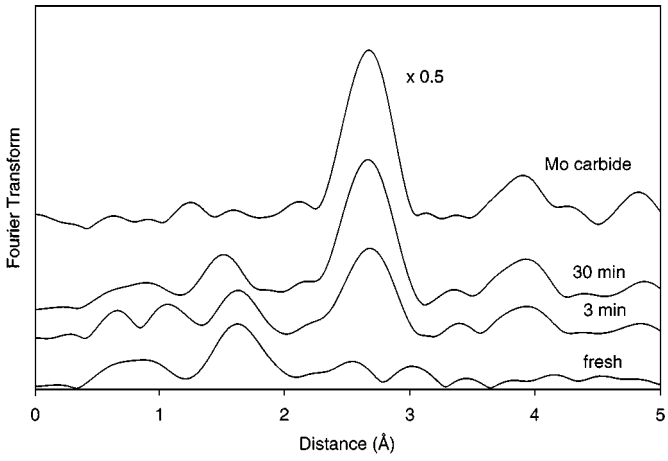

FIG. 21. Fourier transforms of the k^3EXAFS data obtained for the K-edge of Mo for a fresh Co : Mo (1 : 2)/SiO_2 catalyst reduced in hydrogen (500°C), and after the growth of carbon nanotubes for reaction periods of 3 and 30 min. The EXAFS data of Mo_2C are included for comparison.

analysis data of the spent catalyst summarized in Table 6. The best fit of the experimental data was obtained when the coordination sphere of the Mo was described as composed of Mo–C, Mo–Mo, and Mo–O. This indicates that the conversion to Mo carbide is not complete and a fraction of Mo remains in the spent catalyst as an oxidized species.

4. DISCUSSION

4.1. Characteristics of the Calcined Catalysts

The UV–vis and the X-ray absorption data indicate that in all the calcined samples, Mo is in an octahedral environment in the 6+ oxidation state. Furthermore, from the values of the adsorption edge energy it can be concluded that the molybdenum oxide species form small clusters with an average domain size somewhat larger than that of the heptamolybdate ion, but not larger enough to form bulk MoO_3. Regardless of the Co : Mo ratio in the catalysts, the majority of Mo forms these oxidic species. It is apparent that the degree of dispersion of Mo is more a result of the loading and degree of interaction with the support, rather than a consequence of the extent of interaction with Co. A contrasting picture is obtained from the characterization of Co, particularly in the catalysts with low Co : Mo ratio. In this case, both, the UV–vis DRS and the XANES data obtained on the catalyst with a Co : Mo ratio of 1 : 3 demonstrated that most of the Co is in an environment similar to that in α-$CoMoO_4$ (i.e., closely interacting with Mo). However, the slight but clear differences between the spectra of the catalyst and the α-$CoMoO_4$ reference suggest that the similarity is limited to the local environment and nature of ligands. In fact, the EXAFS data demonstrate that bulk α-$CoMoO_4$ is not present in the bimetallic catalysts. Bulk α-$CoMoO_4$ has only been observed by XRD in silica-supported catalysts at high metal contents (14). All these results can be put together in a simple model for the calcined catalysts with low Co : Mo ratios. It can be proposed that Co is in the form of a $CoMoO_4$-like layer on top of Mo oxide species. Therefore, most of the Co is in an interacting phase, while only a fraction of Mo is in such a phase. Therefore, the characterization of Mo does not reflect a strong interaction with Co, while the characterization of Co shows in fact a high degree of interaction with Mo.

In contrast, when the Co is in excess, more than one type of Co species is present in the catalyst. The UV–vis DRS data show that in addition to the interacting phase of Co, which dominates at low Co : Mo ratios, a noninteracting phase begins to form as the Co content increases. The X-ray absorption data (Fig. 6) undoubtedly show that this noninteracting species is Co_3O_4, which has been previously detected by Raman spectroscopy and X-ray diffraction in Co : Mo/SiO_2 catalysts (17, 34).

4.2. Characteristics of the Reduced Catalysts

The DRIFTS data of adsorbed NO give further evidence of the interaction between Co and Mo in the reduced catalysts with low Co : Mo ratios. When the position of the symmetric-stretching band of dinitrosyl adsorbed on Co is compared for the monometallic Co and bimetallic Co-Mo catalysts, a shift of about 8 cm^{-1} to higher wavenumbers is observed with the bimetallic catalyst (Fig. 9). Furthermore, the binding energy obtained by XPS for the fraction of Co that remains unreduced after the reduction treatment in the bimetallic catalyst (around 781.4 eV) corresponds to that of Co interacting with Mo oxide, rather than of a noninteracting Co oxide species (780.1–780.5 eV).

However, as the amount of Co in the reduced catalyst increases, the shift in the IR main band to higher wavenumbers becomes gradually smaller, until the position of the band coincides with that of the monometallic Co/SiO_2 catalyst (i.e., 1803 cm^{-1}). At the same time, the intensity of the band ascribed to the Mo sites gradually decreases, until it practically disappears for the catalyst with a Co : Mo ratio of 2 : 1. This trend is consistent with the XPS data, which indicate that the Mo sites are progressively covered by Co as the Co : Mo ratio increases. Delmon and co-workers have proposed that cobalt molybdate is present in the silica-supported catalyst, and that the noninteracting Co or Mo species (depending on which metal is in excess) agglomerate over $CoMoO_4$, forming a geodelike structure (14). Our results clearly show that when Mo is in excess, this is not the case. The DRIFTS data show that the Co sites are strongly influenced by the presence of Mo but they are not covered by it. On the other hand, a geodelike structure could be postulated for the catalysts in which Co is in excess. That is, Co oxide could partially cover the Co molybdate species.

From the combined analysis of the XPS, TPR, and EXAFS data, one can infer that the reducibility of the Co

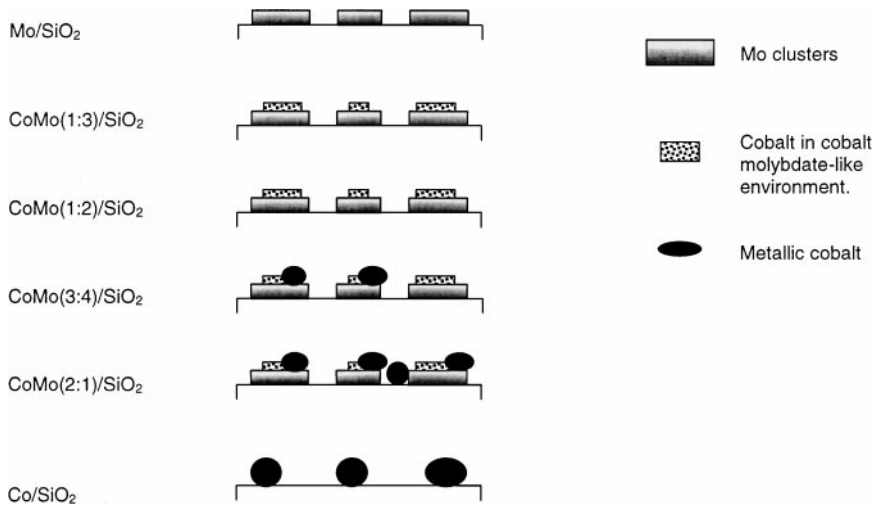

FIG. 22. Schematic description of the structure of the different catalysts in the reduced state before reaction, as derived from the characterization methods.

species is strongly influenced by the presence of Mo in the catalyst. The amount of reducible Co clearly increases with the Co : Mo ratio. This trend can be explained in terms of the formation of an interacting Co molybdatelike species in the oxidized catalyst, which should be more difficult to reduce than noninteracting Co oxide (17). At the same time, as shown in Fig. 12, the reducibility of the Mo species is also affected by the presence of Co, indicating that although the techniques that probe bulk Mo do not show an interaction with Co (XANES, UV–vis DRS), an interaction indeed exists at the catalyst surface and it is more pronounced at low Co : Mo ratios.

Combining all the information obtained from FTIR, XPS, UV–vis DRS, H_2-TPR, and EXAFS/XANES, a coherent representation of the catalyst structure, as it stands right before the beginning of the SWNT reaction, can be put together. This picture is schematically represented in Fig. 22. Three main phases have been identified in the reduced catalyst just before reaction: molybdenum oxide clusters cobalt interacting with molybdenum oxide in a cobalt–molybdate-like structure, partially covering the Mo oxide clusters and segregated metallic cobalt particles. The fraction of each of these species depends on the Co : Mo ratio.

4.3. Relationship between Catalyst Morphology and Selectivity toward SWNT

In previous works (4, 19), we have reported that although MWNT and other carbonaceous forms can be produced from CO disproportionation on monometallic Co catalysts, these catalysts are not selective for the production of SWNT. On the other hand, monometallic Mo catalysts are inactive at the reaction temperatures that we used (around 700–800°C). However, when Co and Mo coexist in the catalysts, especially when Mo is in excess, SWNTs are formed with high selectivity. The results obtained by EXAFS on the spent Co : Mo (1 : 2)/SiO_2 catalyst clearly show that Co suffers a severe transformation under reaction conditions. Before reaction, but after pretreatment in H_2 at 500°C and then in He at 700°C, a considerable fraction of Co is still in the oxide state closely interacting with Mo on the surface, as shown by FTIR, XPS, and EXAFS/XANES. After 3 min under reaction conditions, a significant growth in metallic Co was observed, although some oxidized Co was still present. After 30 min, the particles were even larger and essentially all the Co became metallic. Simultaneously, the Mo that was initially in the oxidized state is converted to the carbidic form, as clearly demonstrated by EXAFS.

As previously proposed (4, 19), the role of Co is the activation of CO. However, when it is in the form of large metal aggregates, it has the tendency to generate mostly MWNT, carbon filaments, and graphite. When Mo is present in the catalyst and there is no Co in excess, a well-dispersed Co^{+2} species in the form of a Co–molybdate-like phase is stabilized. From the detailed studies conducted in this contribution, we can confirm that the formation of this interacting Co–molybdate-like species plays a determinant role in the catalyst selectivity toward the formation of SWNT.

The effect of having Co stabilized on this cobalt-molybdate-like environment is dramatic. First of all, it avoids the reduction and formation of large metallic aggregates. The importance of preventing the reduction of Co is evident when the selective catalyst is compared with a nonselective one (Co : Mo ratio of 2 : 1). In the nonselective catalyst, most of the Co in the oxidic state after calcination is in the form of Co_3O_4 and, as in the monometallic Co/SiO_2 catalyst, this oxide is converted into large metallic Co clusters upon reduction, which produced the unwanted forms of carbon during reaction at 700–800°C. By contrast, on the selective catalyst, a concerted mechanism should take place

during the reaction. As the CO disproportionation starts, Mo oxide is converted into Mo carbide. This transformation breaks up the Co–molybdate-like structure, allowing for the reduction of Co by CO. However, the Co ions are now highly dispersed and in the presence of high concentration of CO in the gas phase. This environment seems to be favorable for the production of SWNT instead of the sintering that would normally occur during a high-temperature reduction process. We may envision the release of extremely small metal Co clusters into the gaseous CO environment in a way that resembles the vapor-phase production of SWNT by the CO disproportionation coupled with decomposition of Fe pentacarbonyl that has been recently developed (47). In that case, like in ours, the production of large metal clusters causes losses in SWNT yield and selectivity.

On the very small Co clusters, the production of MWNT, carbon filaments, and graphite does not occur. Such production normally occurs on larger Co clusters, following the well-known mechanism for carbon filament growth (48). That is, the metal clusters begin to decompose CO, producing Co carbide particles, which then tend to precipitate graphite at their end in the form of cylindrical filaments. When the Co clusters are so small that they are only composed of a few atoms, or even isolated Co atoms, a different mechanism must be considered (49). For instance, a so-called scooter mechanism has been proposed, which takes into consideration the known fact that without a catalyst present, the carbon precursors would tend to grow into C_{60}–fullerenes. However, in the presence of a catalyst, the structure does not close into a hemisphere but is kept open. It has been proposed that metal atoms would diffuse (scoot) along the open edge and prevent the closure of the carbon rings while catalyzing the incorporation of carbon to the growing tube (50). Another model that does not regard the catalyst as isolated atoms, but rather as a metal cluster, has been proposed. In this model, the addition of carbon to the tube occurs at the end of the tube over a metal cluster that is suspended by the growing tube. In this mode, the metal cluster is of the same size or slightly smaller than the diameter of the tube. The metal cluster allows for the stabilization of reactive bonds dangling at the tube tip and prevents the tube closure by moving up with the growing tip (51, 52). When the catalyst particle increases in size, the strain energy of the overcoating becomes smaller, and as a result, the formation of a graphitic overcoat is favored (53).

5. CONCLUSIONS

We can summarize the main findings of the present work in the following conclusions:

(i) The selectivity of the Co-Mo catalysts toward SWNT production by CO disproportionation strongly depends on the stabilization of Co^{2+} species, which result from an interaction with Mo.

(ii) The extent of the Co–Mo interaction is inversely proportional to the Co : Mo ratio and has different forms during the different stages of the catalyst life.

(iii) In the oxidic state after calcination, Mo forms small clusters in the form of well-dispersed Mo (6+) species and Co either interacts with Mo in a superficial Co-molybdate-like structure (at low Co : Mo ratios) or as a noninteracting Co_3O_4 phase (at high Co : Mo ratios).

(iv) During the subsequent reduction treatment, the noninteracting phase is reduced to metallic Co, while the Co–molybdate-like species remain as well-dispersed Co^{2+} ions.

(v) Under reaction conditions, the Mo oxide species are converted into Mo carbide, thus breaking the interaction and releasing the metallic Co in a state of high dispersion, which is responsible for the production of SWNT. By contrast, the large Co clusters are responsible for the nonselective forms of carbon (MWNT, filaments, graphite, etc.).

ACKNOWLEDGMENTS

This research was conducted with financial support from the Oklahoma Center for Advancement of Science and Technology (OCAST) and the College of Engineering at the University of Oklahoma. Technical support from the personnel at NSLS, Brookhaven National Lab, for the EXAFS experiments and from the Noble Electron Microscopy Laboratory at OU for TEM measurements is gratefully acknowledged. The generous technical support of Nicolet Instruments in obtaining the Raman spectra is greatly appreciated. J.E.H. thanks the Fulbright–CAREC program and A.B. thanks Fundacion Antorchas and Fulbright for scholarships.

REFERENCES

1. Yakpbson, B. I., and Smalley, R. E., *Am. Sci.* **85**, 324 (1997).
2. Kong, J. A., Cassel, M., and Dai, H., *Chem. Phys. Lett.* **292**, 567 (1998).
3. Nikolaev, P., Bronikowski, M., Bradley, R., Rohmund, F., Colbert, D., Smith, K., and Smalley, R., *Chem. Phys. Lett.* **313**, 91 (1999).
4. Kitiyanan, B., Alvarez, W. E., Harwell, J. H., and Resasco, D. E., *Chem. Phys. Lett.* **317**, 497 (2000).
5. Lauritsen, J. V., Helveg, S., Lægsgaard, E., Stensgaard, I., Clausen, B. S., Topsøe, H., and Besenbacher, F., *J. Catal.* **197**, 1 (2001).
6. Topsoe, H., and Clausen, B. S., *Catal. Rev. Sci. Eng.* **26**, 395 (1984).
7. Bouwens, S. M. A. M., Prins, R., de Beer, V. H. J., and Koningsberger, D. C., *J. Phys. Chem.* **94**, 3711 (1990).
8. Bouwens, S. M. A. M., van Veen, J. A. R., Koningsberger, D. C., de Beer, V. H. J., and Prins, R., *J. Phys. Chem.* **95**, 123 (1991).
9. Ratnasamy, P., and Knözinger, H., *J. Catal.* **54**, 155 (1978).
10. Wang, L., and Hall, W. K., *J. Catal.* **66**, 251 (1980).
11. Millman, W. S., and Hall, W. K., *J. Phys. Chem.* **83**, 427 (1979).
12. Segawa, K., and Hall, W. K., *J. Catal.* **77**, 221 (1982).
13. Topsøe, N. Y., and Topsøe, H., *J. Bull. Chim. Belg.* **90**, 1311 (1981).
14. Gajardo, P., Grange, P., and Delmon, B., *J. Phys. Chem.* **83**, 1771 (1979).
15. Topsøe, H., Clausen, B. S., Candia, R., Wivel, C., and Mørup, S., *Bull. Soc. Chim. Belg.* **12**, 1187 (1981).
16. Topsøe, H., Clausen, B. S., Burriesci, N., Candia, R., and Mørup, S., *in* "Preparation of Catalysts II" (B. Delmon, P. Grange, P. A. Jacobs, and G. Poncelet, Eds.), p. 479. Elsevier, Amsterdam, 1979.
17. de Boer, M., Koch, E. P. F. M., Blaauw, R. J., Stobbe, E. R., Hoffmann, A. N. J. M., Boot, L. A., van Dillen, A. J., and Geus, J. W., *Solid State Ionics* **63–65**, 736 (1993).
18. Gajardo, P., Pirotte, D., Grange, P., and Delmon, B., *J. Phys. Chem.* **83**, 1780 (1979).

19. Alvarez, W. E., Kitiyanan, B., Borgna, A., and Resasco, D. E., *Carbon* **39**, 547 (2001).
20. Weber, R. S., *J. Catal.* **151**, 470 (1995).
21. Topsøe, N. Y., and Topsøe, H., *J. Catal.* **84**, 386 (1983).
22. Portela, L., Grange, P., and Delmon, B., *Catal. Rev. Sci. Eng.* **37**, 699 (1995).
23. Yao, H. C., and Rothschild, G. W., *in* "Proceedings Climax 4th. International Conference on Chemical Uses of Molybdenum" (H. F. Barry and P. H. Mitchell, Eds.), p. 31. Climax Molybd. Co., Ann Arbor, Michigan, 1982.
24. Kazusaka, A., and Howe, R. F., *J. Catal.* **63**, 447 (1980).
25. Fierro, J. L. G. , *in* "Spectroscopy Characterization of Heterogeneous Catalysis" (J. L. G. Fierro, Ed.), p. B119. Elsevier, Amsterdam, 1990.
26. Prada, R., Fierro, J. L. G., Grange, P., and Delmon, B., *in* "Preparation of Catalysts IV" (B. Delmon, P. Grange, P. A. Jacobs, and G. Poncelet, Eds.), p. 605. Elsevier, Amsterdam, 1987.
27. Clausen, B. S., Lengeler, B., Candia, R., Als-Nielsen, J., and Topsøe, H., *Bull. Soc. Chim. Belg.* **90**, 1249 (1981).
28. Topsøe, H., Clausen, B. S., Topsøe, N. Y., Pedersen, E., Niemann, W., Müller, A., Bögge, H., and Lengeler, B., *J. Chem. Soc., Faraday Trans.* **83**, 2157 (1987).
29. Clausen, B. S., Topsøe, H., Candia, R., Villadsen, J., Lengeler, B., Als-Nielsen, J., and Christensen, F., *J. Phys Chem.* **85**, 3868 (1981).
30. Rehr, J. J., Zabinsky, S. I., and Albers, R. C., *Phys. Rev. Lett.* **69**, 3397 (1992).
31. Rehr. J. J., Mustre de Leon, J., Zabinsky, S. I., and Albers, R. C., *J. Am. Chem. Soc.* **113**, 5135 (1991).
32. Mustre de Leon, J., Rehr, J. J., Zabinsky, S. I., and Albers, R. C., *Phys. Rev. B* **44**, 4146 (1991).
33. Barnton, D. G., Shtein, M., Wilson, R. D., Soled, S. L., and Iglesia, E., *J. Phys. Chem. B* **103**, 630 (1999).
34. Jeziorowski, H., Knözinger, H., Grange, P., and Gajardo, P., *J. Phys. Chem.* **84**, 1825 (1980).
35. Leliveld, R. G., van Dillen, A. J., Geus, J. W., and Koningsberger, D. C., *J. Catal.* **165**, 184 (1997).
36. Xie, S., Chen, K., Bell, A. T., and Iglesia, E., *J. Phys. Chem. B* **104**, 10059 (2000).
37. Halawy, S., Mohamed, M., and Bond, G., *J. Chem Tech. Biotechnol.* **58**, 237 (1993).
38. Kleyna, R., Mex, H., Voß, M., Borgmann, D., Viscido, L., and Heras, J. M., *Surf. Sci.* **433**, 723 (1999).
39. Solymosi, F., Cserényi, J., Szöke, A., Bánsági, T., and Oszkó, A., *J. Catal.* **165**, 150 (1997).
40. Katrib, A., Leflaive, P., Hilaire, L., and Maire, G., *Catal. Lett.* **38**, 95 (1996).
41. Coulier, L., de Beer, V. H. J., van Veen, J. A. R., and Niemantsverdreit, J. W., *Top. Catal.* **13**, 99 (2000).
42. Patterson, T. A., Carver, J. C., Leyden, D. E., and Hercules, D. M., *J. Phys. Chem.* **80**, 1700 (1976).
43. Ebbesen, T. W., and Ajayan, P. M., *Nature* **358**, 220 (1992).
44. Bandow, S. Asaka, S., Saito, Y., Rao, A. M., Grigorian, L., Richter, E., and Eklund, P. L., *Phys. Rev. Lett.* **80**, 3779 (1998).
45. Rols, S., Righi, A., Alvarez, L., Anglaret, E., Almairac, R., Journet, C., Bernier, P., Sauvajol, J. L., Benito, A. M., Maser, W. K., Munoz, E., Martinez, M. T., de la Fuente, G. F., Girard, A., and Ameline, J. C., *Eur. Phys. J. B* **18**, 201 (2000).
46. Rols, S., Righi, A., Alvarez, L., Anglaret, E., Almairac, R., Journet, C., Bernier, P., Sauvajol, J. L., Benito, A. M., Maser, W. K., Munoz, E., Martinez, M. T., de la Fuente, G. F., Girard, A., and Ameline, J. C., *Eur. Phys. J. B* **18**, 201 (2000).
47. Nikolaev, P., Bronikowski, M. J., Bradley, R. K., Rohmund, F, Colbert, D. T., Smith, K. A., and Smalley, R. E., *Chem. Phys. Lett.* **313**, 91 (1999).
48. Tibbetts, G. G., Gorkiewicz, D. W., and Alig, R. L., *Carbon* **31**, 809 (1993).
49. Andriotis, A., Menon, M., and Froudakis, G., *Phys. Rev. Lett.* **85**, 3193 (2000).
50. Thess, A., Lee, R., Nikolaev, P., Dai, H., Petit, P., Robert, J., Xu, C., Lee, Y. H., Kim, S. G., Rinzler, A. G., Colbert, D. T., Scuseria, G. E., Tomanek, D., Fischer, J. E., and Smalley, R. E., *Science* **273**, 483 (1996).
51. Guo, T., Nikolaev, P., Thess, A., Colbert, D. T., and Smalley, R. E., *Chem. Phys. Lett.* **243**, 49 (1995).
52. Maiti, A., Brabec, C., . Roland, C., and Bernholc, J., *Phys. Rev. B* **52**, 14,850 (1995).
53. Dai, H. J., Rinzler, A. G., Nikolaev, P., Thess, A., Colbert, D. T., and Smalley, R. E., *Chem. Phys. Lett.* **260**, 471 (1996).